HHS Public Access

Author manuscript

Acta Biomater. Author manuscript; available in PMC 2022 July 15.

Published in final edited form as:

Acta Biomater. 2021 July 15; 129: 73–83. doi:10.1016/j.actbio.2021.04.048.

Spatially-directed angiogenesis using ultrasound-controlled release of basic fibroblast growth factor from acoustically-responsive scaffolds

Leidan Huang[1,2], **Carole Quesada**[2], **Mitra Aliabouzar**[2], **J. Brian Fowlkes**[2,3,4], **Renny T. Franceschi**[3,5], **Zheng Liu**[1,*], **Andrew J. Putnam**[3], **Mario L. Fabiilli**[2,3,4,*]

[1]Department of Ultrasound, Second Affiliated Hospital of Army Medical University, Chongqing, China

[2]Department of Radiology, University of Michigan, Ann Arbor, MI, USA

[3]Department of Biomedical Engineering, University of Michigan, Ann Arbor, MI, USA

[4]Applied Physics Program, University of Michigan, Ann Arbor, MI, USA

[5]Dental School, University of Michigan, Ann Arbor, MI, USA

Abstract

Vascularization is a critical step following implantation of an engineered tissue construct in order to maintain its viability. The ability to spatially pattern or direct vascularization could be therapeutically beneficial for anastomosis and vessel in-growth. However, acellular and cell-based strategies to stimulate vascularization typically do not afford this control. We have developed an ultrasound-based method of spatially-controlling regenerative processes using acellular, composite hydrogels termed acoustically-responsive scaffolds (ARSs). An ARS consists of a fibrin matrix doped with a phase-shift double emulsion (PSDE). A therapeutic payload, which is initially contained within the PSDE, is released by an ultrasound-mediated process called acoustic droplet vaporization (ADV). During ADV, the perfluorocarbon (PFC) phase within the PSDE is vaporized into a gas bubble. In this study, we generated ex situ four different spatial patterns of ADV within ARSs containing basic fibroblast growth factor (bFGF), which were subcutaneously implanted in mice. The PFC species within the PSDE significantly affected the morphology of the ARS, based on the stability of the gas bubble generated by ADV, which impacted host cell migration. Irrespective of PFC, significantly greater cell proliferation (i.e., up to 2.9-fold) and angiogenesis (i.e., up to 3.7-fold) were observed adjacent to +ADV regions of the ARSs compared to −ADV regions. The morphology of the PSDE, macrophage infiltration, and perfusion in the implant

[*]**Corresponding Authors:** Mario Fabiilli, Ph.D., University of Michigan, 1301 Catherine Street, 3226A Medical Sciences Building I, Ann Arbor, MI 48109-5667, mfabiill@umich.edu, Zheng Liu, M.D., Ph.D., Army Medical University, The Second Affiliated Hospital, 183 Xinqiao Street, Shapingba District, Chongqing 400037, liuzhengs@hotmail.com.

Declaration of interests

☒ The authors declare that they have no known competing financial interests or personal relationships that could have appeared to influence the work reported in this paper.

region were also quantified. These results demonstrate that spatially-defined patterns of ADV within an ARS can elicit spatially-defined patterns of angiogenesis. Overall, these finding can be applied to improve strategies for spatially-controlling vascularization.

Graphical Abstract

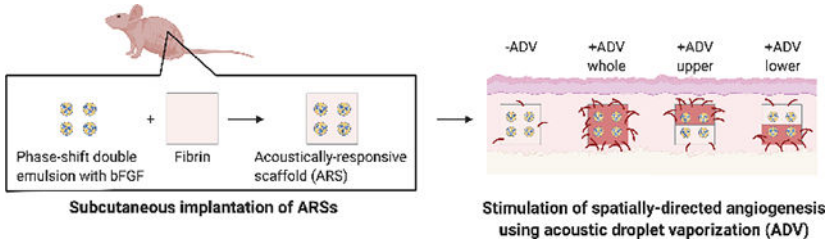

Keywords

angiogenesis; basic fibroblast growth factor; fibrin; ultrasound; acoustic droplet vaporization; drug delivery

1. Introduction

Vascularization is required to integrate an engineered tissue construct with the blood supply of the host upon *in vivo* implantation. However, spontaneous in-growth of vessels into constructs can be slow (e.g., less than 5 μm per hour [1, 2]), which can lead to cellular necrosis and an overall reduction in construct viability. To stimulate vascularization, acellular and cell-based strategies have been investigated. With the former, pro-angiogenic growth factors [3] or genes for these factors [4] have been delivered within implantable scaffolds. With the latter, scaffolds containing cells involved in vascularization (e.g., endothelial, stromal, and/or mesenchymal stem cells) [5] or preformed vascular networks [6] have been tested.

The ability to spatially pattern or direct vascularization could be therapeutically beneficial for inosculation and blood vessel in-growth. However, conventional methods of incorporating pro-angiogenic molecules, cells, or vascular networks within scaffolds do not typically yield spatially-controlled vascularization. Thus, efforts rely on *a priori* patterning techniques of the aforementioned entities. For example, bilayer poly(lactide-co-glycolide) scaffolds were fabricated with different loadings of vascular endothelial growth factor (VEGF) in each layer; after *in vivo* implantation, the density of vessels surrounding each layer of the scaffold was commensurate with the VEGF loading in the layer [7]. Using laser scanning lithography, an integrin ligand (i.e., RGDS) and VEGF were covalently patterned onto the surface of a poly(ethylene glycol) (PEG) hydrogel, thereby leading to spatially patterned *in vitro* tubulogenesis [8]. Another approach has been to spatially pattern different levels of crosslinking within a hyaluronic acid hydrogel using ultraviolet light, thereby rendering areas of low and high matrix degradability that were inhibitory and permissive, respectively, to *in vitro* vasculogenesis and angiogenesis [9]. 3D bioprinting has also been used to control the spatial pattern of engineered vessels, either by direct printing of cells

within a hydrogel or by seeding cells within printed channels. Tubes of vascular smooth muscle cells were printed in a gelatin methacryloyl/PEG diacrylate/alginate hydrogel followed by seeding of vascular endothelial cells within the lumens [10]. Endothelial cells were seeded into fibrin channels created by the dissolution of printed, sacrificial sugar filaments; the spatial pattern of the vascular network impacted perfusion recovery in rodent cardiovascular models [11].

Ultrasound (US), which is used clinically in both diagnostic and therapeutic applications, is an attractive modality for modulating regenerative processes like angiogenesis since US can be applied non-invasively, focused with submillimeter precision, and delivered at depth in a spatiotemporally-controlled manner. Previously, US standing waves have generated spatially aligned layers of myofibroblasts and neural progenitor cells within collagen [12] and fibrin hydrogels [13], respectively. Additionally, US standing waves were used to create fabricated vessels consisting of aligned cylindroids of endothelial cells and adipose-derived stem cells within catechol-conjugated hyaluronic acid hydrogels [14]. In these US-based approaches, US was applied during the polymerization of the construct, which including the necessity of a standing wave field, make these techniques most realizable for spatially controlling cell alignment *in vitro* or *ex situ*.

We have developed an US-based method for controlling regenerative processes via the release of growth factors from acellular, composite hydrogels termed acoustically-responsive scaffolds (ARSs) [15, 16]. This technique is amenable both *in vitro* and *in vivo*, including after implantation of the ARS that would ultimately enable personalization of therapy. An ARS consists of a fibrin hydrogel doped with a phase-shift double emulsion (PSDE) with a water-in-perfluorocarbon (PFC)-in-water structure (i.e., W_1/PFC/W_2). The growth factor payload, which is contained within the inner W_1 droplets, is dispersed within a hydrophobic PFC phase that inhibits diffusion of the payload from the PSDE [17]. The encapsulated payload is selectively released when the morphology of the PSDE is disrupted by the US-triggered phase transition of the PFC – a process known as acoustic droplet vaporization (ADV) [18]. ADV is threshold dependent and only occurs when the PSDE is exposed to US with a rarefactional (i.e., tensile) pressure exceeding the ADV threshold. ADV is triggered by pulsed US with a low duty cycle, thereby preventing any US-induced heating [19, 20]. The survival of the bubble generated by ADV is dependent on the PFC used to formulate the PSDE (Figure 1A) [21, 22]. With lower boiling point species such as perfluorohexane (C_6F_{14}), ADV generates stable gas bubbles that remain trapped within the ARS. With higher boiling point PFCs like perfluorooctane (C_8F_{18}), the gas bubble recondenses.

Previously, ARSs have been used for the controlled release of basic fibroblast growth factor (bFGF), a protein that stimulates many processes such as proliferation and angiogenesis [23, 24]. bFGF has been tested clinically in patients with ischemic cardiovascular disease [25] or chronic skin ulcers [26]. The stability of bFGF in the bloodstream is poor [27] and systemic doses can cause adverse effects [28]. This has motivated efforts to improve its efficacy and safety via controlled delivery using implantable biomaterials. Using ARSs, ADV triggered release of bFGF has been shown to stimulate fibroblast proliferation [29] and endothelial network formation [30] *in vitro* as well as cell migration [31] and angiogenesis [29] *in vivo*.

Here we present a method for eliciting a spatially-directed, angiogenic response from the host upon *in vivo* implantation of an ARS (Figure 1B). ARSs were generated with bFGF-loaded PSDE and exposed to US *ex situ* to generate four different spatial patterns of ADV. The ARSs were subcutaneously implanted in mice and perfusion in the implant region was longitudinally measured using laser speckle contrast analysis (LASCA) imaging. After 14 days, the following parameters were evaluated using histological staining: overall scaffold morphology, PSDE morphology, cell proliferation, angiogenesis, and macrophage infiltration. As will be shown, spatially-defined patterns of ADV yielded spatially-directed patterns of cell proliferation and angiogenesis.

2. Materials and Methods

2.1 Preparation and characterization of PSDE

PSDEs containing bFGF were prepared by modifying a previously described method [29]. A triblock fluorosurfactant, consisting of Krytox 157FSH (CAS# 51798–33-5, DuPont, Wilmington, DE, USA) and polyethylene glycol (1000 g/mol, CAS#: 24991–53-5, Alfa Aesar, Ward Hill, MA USA), was dissolved at 2% (w/w) in perfluorohexane (C6, CAS#: 355–42-0, Strem Chemicals, Newburyport, MA USA) or perfluorooctane (C8, CAS#: 307–34-6, Alfa Aesar). Each PFC phase was combined at 2:1 (v/v) with a W_1 phase containing 3.6 mg/mL recombinant human bFGF (Cat#: GF003AF, EMD Millipore, Temecula, CA USA), 10 mg/mL bovine serum albumin (Sigma-Aldrich, St. Louis, MO USA), and 20 μg/mL heparin (Cat #: 375095, Calbiochem, San Diego, CA, USA) in phosphate-buffered saline (PBS, Life Technologies, Grand Island, NY USA). The phases were sonicated (Q55 with a CL-188 immersion probe, QSonica, Newton, CT, USA) for 30 sec while on ice.

To generate each PSDE, the primary emulsion and a W_2 phase consisting of 50 mg/mL Pluronic F68 (CAS# 9003–11-6, Sigma-Aldrich) in PBS were pumped at 1 μL/min and 10 μL/min, respectively, onto a glass microfluidic chip with a flow focusing junction (Cat#: 3200136, junction: 14 × 17 μm, hydrophilic coating, Dolomite, Royston, United Kingdom). Each phase was passed through an in-filter (Cat# 24993, Restek, Bellefonte, PA, USA) prior to entering the chip. The PSDEs were characterized using a Coulter counter (Multisizer 4, Beckman Coulter, Brea, CA USA) with a 50 μm aperture (Supplemental Figure 1). The average diameter, coefficient of variation, and concentration of the C6-PSDE (N=3) were 10.5 ± 1.9 μm, 27.9 ± 2.7%, and (0.9 ± 0.6) × 10^9 droplets/mL, respectively. For the C8-PSDE (N=3), the average diameter, coefficient of variation, and concentration were 6.9 ± 1.1 μm, 21.4 ± 8.1%, and (3.5 ± 0.9) × 10^9 droplets/mL, respectively. The differences in sizing parameters were not statistically significant between the two emulsions.

2.2 Preparation of ARSs and control scaffolds

Scaffolds were polymerized within custom, multi-well plates made by machining 9.5 mm diameter holes in a sheet of poly(methyl methacrylate) (85 mm × 125 mm × 5.5 mm). A Tegaderm membrane (3M HealthCare, St. Paul, MN USA) was adhered to the bottom of the sheet to create a well bottom. The wells were blocked with 10 mg/mL bovine serum albumin for at least 30 minutes to facilitate later removal of the scaffolds.

Bovine fibrinogen (Sigma-Aldrich) was prepared at 20 mg/mL clottable protein in Dulbecco's modified Eagle's medium (DMEM, Thermo Fisher Scientific, Waltham, MA, USA). Bovine lung aprotinin (Sigma-Aldrich) was added at 0.1 U/mL and the solution was degassed in a vacuum chamber to facilitate complete dissolution of the fibrinogen and to minimize the presence of bubbles. ARSs (total volume = 0.3 mL, diameter = 9.5 mm, height = 4.2 mm) were prepared by combining the fibrinogen solution, DMEM, bovine thrombin (Thrombin-JMI, Pfizer, New York, NY, USA), as well as PSDE and aliquoting the mixture into the well plate. The final concentrations of fibrinogen, aprotinin, thrombin, and PSDE were 10 mg/mL, 0.05 U/mL, 2 U/mL and 2.8% (v/v), respectively. Each ARS nominally contained 10 μg bFGF. The ARSs were allowed to polymerize for 15 minutes at room temperature. ARSs containing C6- and C8-PSDEs are referred to as C6-ARSs and C8-ARSs, respectively. Control scaffolds consisting of only fibrin or fibrin containing 10 μg of unencapsulated bFGF (i.e., fibrin+bFGF) were prepared similarly.

For ARSs where ADV was generated in a subvolume of the scaffold (i.e., +ADV upper, +ADV lower), the ARS was polymerized using a two-step, bilayer approach. An ARS of one half volume (i.e., 0.15 mL) was polymerized, sealed within the plate, and exposed to US to generate ADV (methods described in the subsequent section). Following US exposure, another ARS of one half volume was overlaid and polymerized on top of the first layer.

2.3 US exposure

ARSs were exposed to US in a water tank (30 cm × 60 cm × 30 cm) filled with degassed (12–22% O_2 saturation), deionized water at 37°C. A calibrated, focused, single-element US transducer (H147, 2.5 MHz, f-number = 0.83, radius of curvature = 50 mm, Sonic Concepts, Inc., Bothell, WA USA) was used to generate ADV within the ARSs. The transducer was connected to a three-axis positioning system controlled by MATLAB (The MathWorks, Natick, MA, USA).

The transducer was driven by pulsed waveforms generated using a waveform generator (33500B, Agilent Technologies, Santa Clara, CA, USA) and amplified by a gated radiofrequency amplifier (GA-2500A Ritec Inc, Warwick, RI, USA). The amplified waveform was passed through a matching circuit (H108_3 MN, Sonic Concepts) to reduce the impedance mismatch between the transducer and amplifier. Waveforms were monitored with an oscilloscope (HDO4034, Teledyne LeCroy, Chestnut Ridge, NY, USA). To generate ADV within the ARSs, the following acoustic parameters were used: 6.1 MPa peak rarefactional pressure, 5.4 μs pulse duration, and 100 Hz pulse repetition frequency. This peak rarefactional pressure was previously shown to be suprathreshold for ADV within the ARSs [21]. During US exposure, the transducer was rastered at a speed of 5 mm/s with a 0.5 mm lateral spacing between raster lines. Exposures were done at three axial planes located 3 mm, 2 mm, and 1 mm above the well bottom, with exposures completed from the top/distal (i.e., 3 mm) to bottom/proximal (i.e., 1 mm) direction. The time required to complete the US exposure for each ARS was approximately 2 min.

2.4 In vivo implantation of scaffolds

This *in vivo* research was conducted with the approval of the Institutional Animal Care & Use Committee (IACUC) at the University of Michigan. Hairless, immunocompetent SKH1-Elite mice (female, n = 25, 4–6 weeks old, 21.0 ± 2.0 g, Charles River Laboratories, Wilmington, MA, USA) were anesthetized with isoflurane (5% for induction and 1.5% for maintenance). The skin was disinfected with povidone-iodine (Betadine, Purdue Products, Stamford, CT, USA). Two full thickness skin incisions approximately 1 cm in length were made in the lower dorsal region parallel to and on either side of the spine. Small pouches were bluntly dissected in the subcutaneous tissue and one scaffold was implanted in each pouch. The wounds were closed with interrupted silk sutures (6–0, Ethicon, New Brunswick, NJ, USA). With ARSs, four different spatial patterns of ADV were interrogated. For single layer ARSs, −ADV and +ADV whole patterns were tested. For bilayer ARSs, ADV was generated in one layer of the ARS and then implanted such that the +ADV layer was either proximal to the skin (i.e., +ADV upper) or underlying muscle (i.e., +ADV lower).

2.5 Evaluation of perfusion

Perfusion in the implant region was measured on day 0 (i.e., immediately after implantation), 1, 3, 7, 10, and 14 using a PeriCam PSI HR (Perimed, Ardmore, PA USA) laser speckle contrast analysis (LASCA) system. During imaging, mice were anesthetized with isoflurane and placed in a lateral recumbent position on a heated (i.e., 37°C) water blanket to enable imaging of one of the implanted scaffolds. All images were acquired with a 10 cm distance between the scanner and mouse, resulting in a resolution of 20 μm/pixel. Pimsoft software (Perimed) was used for image acquisition and processing. A total of 30 images per anatomical location per time point were acquired at a rate of 0.096 images/s with a field of view of 2.0 × 2.8 cm. Every 6 images were averaged to create a total of five averaged images per location per time point. Three of the five averaged images were used for perfusion analysis. The average relative perfusion was calculated within a circular (diameter: 0.5 cm) region of interest (ROI) placed in the implant region. The change in average perfusion, relative to day 0, was subsequently computed.

2.6 Histological analyses

Mice were euthanized on day 14 post implantation. The implants were harvested with the surrounding tissue and fixed overnight in aqueous buffered zinc formalin (Formalde-Fresh, Fisher Scientific). Tissue samples were transferred into 70% (v/v) ethanol until processing and embedding in paraffin by the Tissue & Molecular Pathology Core at the University of Michigan. Serial sections (thickness: 5 μm) were cut from the embedded tissue and transferred onto pre-cleaned glass slides (Fisherbrand Superfrost Plus, Thermo Fisher Scientific) for histological analyses. Tissue sections were stained with hematoxylin and eosin (H&E) to visualize the overall tissue morphology. Tissue sections were immunohistochemically stained using a rabbit anti-mouse Ki-67 primary antibody (ab15580, Abcam, Cambridge, MA USA), rabbit anti-mouse CD31 primary antibody (ab182981, Abcam), rabbit anti-mouse bFGF primary antibody (ab92337, Abcam), and rabbit anti-mouse CD68 primary antibody (ab125212, Abcam). A goat anti-rabbit secondary labeled polymer-horseradish peroxidase conjugate (Envision+ System-HRP (DAB), Dako North

America, Inc., Carpinteria, CA USA) was used with all primary antibodies. Staining specificity was confirmed by staining with only the secondary conjugate.

Stained tissue sections were imaged with an inverted microscope (Eclipse Ti-E, Nikon, Melville, NY, USA) with 4x and 20x objectives, color digital camera (DS-Fi3, Nikon), and associated software (NIS-Elements, Nikon). At the higher magnification, five fields of view per tissue section were acquired in the upper and lower implant regions that captured the implant-tissue interface and surrounding granulation tissue. Host cell migration into the ARS was determined from the H&E images by measuring the distance cells traversed the initially acellular implant from the ARS-host interface; a distance of zero indicated no cell migration. Ki-67, bFGF, and CD68 images were analyzed in ImageJ (National Institutes of Health, Bethesda, MD, USA) using custom macros that included a color deconvolution plugin [32]. The following parameters were obtained: the density of Ki-67+ cells, the average diameter of bFGF+ PSDE droplets within the ARS, the density of bFGF+ PSDE droplets within the ARS, the area percent of the ARS that stained bFGF+, and the area percent of tissue that stained CD68+. The density of blood vessels, defined as CD31+ structures possessing a lumen, were determined by trained readers in a blinded manner. For parameters derived from Ki-67, CD31, and CD68 staining, upper and lower regions were characterized from the panniculus carnosus to the ARS-host interface and from the ARS-host interface to the underlying skeletal muscle, respectively. For parameters derived from bFGF staining, upper and lower regions were characterized within the ARS relative to the corresponding ARS-host interface.

2.7 Statistics

Statistical analyses were performed using GraphPad Prism software (GraphPad Software, Inc., La Jolla, CA USA). All data are expressed as the mean ± standard error of the mean of measured quantities. The number of independent replicates (N) is listed within each figure caption

Significant differences between groups were determined using a one-way ANOVA followed by Tukey's multiple comparisons test. A significance level of 0.05 was used. For histomorphometric parameters, significant differences are indicated as follows. Significant differences in the lower region are denoted by: α: vs. fibrin; β: vs. fibrin + bFGF; γ: vs. ARS (−ADV); δ: vs. ARS (+ADV whole); and ε: vs. ARS (+ADV upper). In the upper region, significant differences are by: ζ: vs. fibrin; η: vs. fibrin + bFGF; θ: vs. ARS (−ADV); ι: vs. ARS (+ADV whole); and κ: vs. ARS (+ADV upper). Significant differences between PFC species are denoted by λ and μ for the lower and upper regions, respectively. Significant differences among the LASCA data are denoted as follows: α: fibrin vs. C6-ARS (+ADV whole); β: fibrin + bFGF vs. C6-ARS (+ADV whole); γ: fibrin vs. C6-ARS (−ADV); δ: fibrin vs. C6-ARS (+ADV upper); ε: fibrin + bFGF vs. C6-ARS (+ADV upper); ζ: C8-ARS (−ADV) vs. C8-ARS (+ADV upper); η: C8-ARS (−ADV) vs. C8-ARS (+ADV lower); θ: C8-ARS (+ADV whole) vs. C8-ARS (+ADV lower); and ι: fibrin + bFGF vs. C8-ARS (+ADV lower).

3. Results

3.1 ARS morphology and cell migration

The overall morphologies of the ARSs can be observed in H&E images (Figure 2A, Supplemental Figure 2). In the absence of ADV, the C6-ARSs and C8-ARSs appear relatively homogeneous. Round, micron-sized voids are visible due to the presence of unactivated PSDE within the fibrin matrix. After ADV in C6-ARSs, large voids within the fibrin matrix are visible, which are due to stable gas bubbles formed from C6-PSDE. The pattern of bubble formation correlated with the pattern of ADV. Morphological changes were more subtle in C8-ARSs following ADV. The micron-sized voids appear irregularly shaped and slightly larger in size compared to the −ADV condition as well as correlated with the pattern of ADV.

The distances that host cells migrated into the ARSs were quantified (Figure 2B). There was significantly less migration (i.e., up to 1.9-fold; $p < 0.0001$) in all C6-ARS conditions compared to fibrin only and fibrin+bFGF groups. There was no correlation between cell migration and the pattern of ADV for C6-ARSs. Comparatively, there was significantly greater cell migration (i.e., up to 1.8-fold ($p = 0.01$) and 2.1-fold ($p < 0.0001$) in the lower and upper regions, respectively) in +ADV regions of C8-ARSs compared to control scaffolds. In general, cell migration correlated with the pattern of ADV in C8-ARSs. For example, for the +ADV upper pattern, there was significantly greater migration (i.e., 1.6-fold; $p = 0.0008$) in the upper region compared to the lower region. Additionally, there was 2.1-fold greater migration in the upper region when comparing +ADV upper versus +ADV lower patterns ($p = 0.0001$). When comparing C6-ARSs with C8-ARSs, there was greater migration in most regions for the latter ARSs.

The morphology of the PSDE was evaluated by immunohistochemical staining of the bFGF payload (Figure 3A, Supplemental Figure 3). Similar to the H&E images, the PSDE appear as round, micron-sized structures with bFGF+ staining in the −ADV groups. For the +ADV groups with C6-ARSs, intact (i.e., unvaporized) PSDE is visible within both the −ADV and +ADV regions, including matrix regions surrounding the generated bubbles. In C8-ARSs, the PSDE became more irregularly shaped and qualitatively larger in size in +ADV regions.

Based on the bFGF stained images, the following parameters were quantified: PSDE droplet diameter (Figure 3B), PSDE droplet density (Figure 3C), and bFGF+ area percent (Figure 3D). The droplet diameters measured for −ADV conditions for both C6- and C8-ARSs (Figure 3B) were not statistically different than the initial sizing values obtained for the PSDEs using a Coulter counter. There were no significant differences among any of the C6-ARS conditions or regions. With C8-ARSs, there were significant differences that indicated an increase in droplet size following ADV. For example, for the +ADV lower pattern, droplets within the lower region were 39% larger than those in the upper region ($p = 0.02$), as well as larger compared to the lower regions of the −ADV (i.e., 27%; $p = 0.01$) and +ADV upper (i.e., 33%; $p = 0.003$) patterns. With both C6- and C8-ARSs, there were significantly less droplets in +ADV regions compared to −ADV regions (Figure 3C). For example, when comparing −ADV and +ADV whole patterns, there were up to 75% ($p = 0.0006$) and 70% ($p < 0.0001$) decreases in density for C6-ARSs and C8-ARSs, respectively. When comparing

identical patterns of ADV and regions, there were significantly more droplets for C8-ARSs in some instances. However, this is likely due to initial differences in PSDE density. Though not significantly different, there was a trend for a greater droplet density with C8- versus C6-PSDE. A similar correlation was also observed with bFGF+ area (Figure 3D), where generally, - ADV regions displayed significantly greater area compared to +ADV regions.

3.2 Cell proliferation and angiogenesis

Cell proliferation around the implants was assessed using immunohistochemical staining of Ki-67 (Figure 4A, Supplemental Figure 4). Ki-67+ cells were present within the granulation tissues surrounding the implants as well as host cells that had migrated into the implants. The density of Ki-67+ cells was also quantified (Figure 4B). With C6-ARSs, significantly higher densities of proliferating cells were observed in all +ADV regions compared to fibrin only and fibrin+bFGF groups. Overall, greater proliferation was observed adjacent to +ADV regions of the ARSs compared to −ADV regions. For example, with the +ADV lower pattern in C6-ARSs, the density of Ki-67+ cells in the lower region was significantly greater (i.e., 2.9-fold; $p = 0.0007$) than in the upper region. Additionally, with C6-ARSs, there was 2.6-fold more proliferation in the upper region of the +ADV upper pattern compared to the upper region of the +ADV lower pattern ($p = 0.0009$). A similar correlation between +ADV regions and cell proliferation was seen with C8-ARSs, though slightly less obvious than with C6-ARSs. There were no differences between C6- and C8-ARSs when comparing identical patterns of ADV and tissue regions. Furthermore, there were no significant differences when comparing the −ADV condition for C6- and C8-ARSs versus fibrin only and fibrin+bFGF groups.

Angiogenesis was assessed by immunohistochemically staining the tissue samples for CD31 (Figure 5A, Supplemental Figure 5). The density of blood vessels, which were visible within the granulation tissues surrounding the implants, was quantified (Figure 5B). The trends observed with angiogenesis were similar to those observed with cell proliferation. In general, significantly higher vessel densities were observed adjacent to +ADV regions of the ARSs compared to corresponding −ADV regions. For C6-ARSs, the lower and upper regions of the +ADV whole pattern displayed 2.8- and 4.2-fold more vessels than the same regions of the −ADV condition ($p = 0.003$; $p < 0.0001$). Tissue proximal to the +ADV regions of the +ADV lower and +ADV upper exhibited 2.7- and 3.6-fold greater angiogenesis than the corresponding distal areas adjacent to −ADV regions ($p = 0.02$; $p = 0.01$). With the +ADV upper pattern, there were significantly more vessels (i.e., 2.7-fold; $p = 0.0002$) in the upper region compared to the upper region of the +ADV lower pattern. Analogously, with the +ADV lower pattern, the vessel density was 3.7-fold higher in the lower region compared to the same region with the +ADV upper pattern ($p = 0.0001$). Similar findings were also seen with C8-ARSs.

3.3 Perfusion

In addition to the morphological evaluation of angiogenesis at day 14, perfusion in the implant region was longitudinally monitored by non-invasive LASCA imaging (Figure 6A, Supplemental Figure 6). The change in perfusion in the implant region was quantified using ROIs (Figure 6B). With C6-ARSs, there was a greater decrease in perfusion on day 1 for all

ARS groups compared to fibrin only and fibrin+bFGFs implants, with differences deemed significant for −ADV and +ADV whole patterns. The maximum change in perfusion for fibrin only and fibrin+bFGF groups was observed on day 7. With the C6-ARS groups, the maximum perfusion was observed on day 14 for −ADV, +ADV whole, and +ADV upper patterns, with significant increases relative to control scaffolds seen with the latter two groups. There were overall smaller changes in perfusion with C8-ARSs compared to C6-ARSs.

3.4 Macrophage infiltration

The presence of macrophages in and around the scaffolds was evaluated by immunohistochemical staining of CD68 (Supplemental Figure 7A). Based on a quantitative analysis of the images, no significant differences were observed between any of the groups (Supplemental Figure 7B).

4. Discussion

The PFC species within the PSDE dramatically impacted the morphology of the ARS after ADV and cell migration into the ARS. Based on classical nucleation theory, the threshold bubble radius above which an ADV-generated bubble remains stable against condensation is 5.2 μm for C6-bubbles [22]. The average diameter of the C6-PSDE used in this study was larger than this threshold radius, thereby facilitating stable gas bubble formation. Irrespective of size, a C8-bubble recondenses at physiological conditions due to its high supersaturation ratio, which is the ratio of the vapor pressure within the bubble versus the equilibrium vapor pressure. Despite the release of bFGF by ADV, stable bubbles within the C6-ARSs hindered migration of host cells into the scaffold, which were previously determined to be primarily fibroblasts and myofibroblasts [31]. Following ADV in C6-ARSs, coalescence [33, 34] and in-gassing [18, 35] of the generated bubbles yielded sizes that were larger than the value predicted based on an estimate using the ideal gas law for the vaporization of micron-sized droplets (i.e., 46 μm), which does not account for either mechanism. In C8-ARSs, ADV caused coalescence of the PSDE as seen with the increase in droplet diameter based on bFGF staining. Previously, expulsion of the W_1 phase by ADV caused a decrease in the average droplet diameter within a C8-ARS containing 0.005% (v/v) PSDE [22]. In this study, a higher concentration of PSDE within the C8-ARS (i.e., 2.8% (v/v)) increased the likelihood for neighboring droplets to coalesce during ADV due to a smaller inter-droplet spacing. With C8-ARSs, cell migration was significantly enhanced by the release of bFGF with ADV and correlated with the pattern of ADV.

Stable bubbles within ARSs impact other properties such as matrix compaction, degradation, and payload diffusion. For example, ARSs with PSDE containing perfluoropentane, which is more volatile than C6, expanded considerably *in vitro* following ADV [21]. Stable bubbles within C6-ARSs were also shown to inhibit overall matrix compaction *in vivo* compared to C8-ARSs that compacted significantly [31]. Bubbles generated within C6-ARSs have been shown to induce localized compaction and stiffening of the fibrin matrix adjacent to the bubble, which was attributed to the strain stiffening behavior of fibrin [36]; irreversible changes to matrix compaction were also observed in C8-ARSs after ADV, though changes

were more subtle. Consistent with these structural and mechanical changes in C6-ARSs, stables bubbles also inhibited fibrin degradation *in vitro* [37], though this effect was not observed *in vivo* [38]. The rate of payload diffusion was also inversely related to the concentration of bubbles within the ARS for payloads with minimal (e.g., dextran [21, 37]) and high (e.g., bFGF [30, 31]) binding affinities for fibrin.

The highest levels of proliferation and angiogenesis were observed adjacent to +ADV regions of the ARSs, though neither metric displayed a dependence on the PFC species within the ARS. This is similar to previous studies where the angiogenic response stimulated by acellular fibrin scaffolds containing VEGF [3] or bFGF [39] was within the tissue surrounding the subcutaneous implant, and not within the implant itself. Overall, regions that displayed high densities of proliferating cells also exhibited high levels of angiogenesis, which is consistent with the pleotropic effects of bFGF [40]. Compared to the fibrin + bFGF group, significantly greater proliferation and angiogenesis were observed adjacent to the +ADV regions of the ARSs, which is attributed to a slower rate of release of bFGF from the ARSs [30, 31, 37]. Sustained release of bFGF has been shown to enhance angiogenesis relative to burst release [41, 42]. Additionally, the lack of differences in CD68 staining suggests that the PSDE did not significantly change properties of the fibrin matrix in regards to macrophage infiltration [43].

For C6-ARSs, the changes in perfusion measured by LASCA imaging on day 14 correlated with immunohistochemical quantification of angiogenesis, as demonstrated previously with other subcutaneous implants [44]. The +ADV whole and +ADV upper patterns displayed the largest change in perfusion as well as high densities of blood vessels adjacent to +ADV regions. Comparatively, there was a high density of vessels in the +ADV region of the +ADV lower pattern, but an insignificant change in perfusion. This could be related to the penetration depth of the laser, which is in the range of 0.5–1 mm depending on the optical properties of the tissue [45]. Thus, changes in blood vessel density and corresponding perfusion at greater depths would not be detectable based on LASCA imaging. Interestingly, with C8-ARSs, there were no correlation between measured perfusion on day 14 and angiogenesis, despite having vessel densities that were not statistically different than the corresponding C6-ARSs. There are four potential explanations for this. First, LASCA imaging measures perfusion within the tissue, irrespective of whether the vessels are new or pre-existing. In addition to stimulating angiogenesis, bFGF can also impact arteriogenesis [46] which would impact pre-existing vessels and thus not necessarily increase vessel density. Second, LASCA imaging relies on measuring backscattered signal [47]. Due to differences in bubble formation in C6- and C8-ARSs, the optical properties of the ARS could be impacting the backscattered signal. Third, differences in the thickness of the granulation tissue overlying the ARSs could be impacting the LASCA imaging, as described previously in terms of laser penetration depth. However, in this study (data not shown) as well as others [31, 38], there were no significant differences in the thickness of the granulation tissue. Fourth, CD31 staining confirms the structural presence of vessels whereas LASCA images measures perfusion. Vessels can remain structurally intact prior to flow-mediated pruning and regression [48].

There are important factors to consider when comparing C6- versus C8-ARSs for regenerative applications, which are closely linked to the formation of stable versus transiently-stable bubbles. C8-ARSs facilitated host cell migration into the scaffold compared to C6-ARSs. Thus, in scenarios where host cell migration is critical or if cells are encapsulated into the ARS, it could be beneficial to minimize bubble formation or to spatially localize bubble formation to influence cell behavior. Following ADV, the rate of payload release is slower in C6-ARSs compared to C8-ARSs [31], which could be beneficial in maintaining the microenvironmental concentration of growth factors [49]. The ADV threshold in C6-ARSs is lower than in C8-ARSs [21], thus requiring lower acoustic amplitudes to achieve payload release with the former ARSs. ADV can be achieved in C6-ARSs using higher frequency ultrasound [22], thus enabling tighter localization of ADV and the minimization of cavitation-related bioeffects.

A limitation of this study was the use of bilayer ARSs in combination with *ex situ* US to generate the +ADV upper and +ADV lower patterns. This approach enabled precise patterning of ADV within the respective layers. *In situ* patterning could be achieved with real-time US image guidance such as cavitation mapping [50]. Based on the size of implants used in mouse models, spatial patterning of ADV in the lateral dimension, versus the axial direction as was done in this study, would be most realizable.

5. Conclusions

An US-based method termed ADV was used to modulate the release of bFGF from an ARS, which caused a decrease in the density of PSDE within the scaffold. Following ADV, the molecular weight of the PFC component of the PSDE significantly impacted scaffold morphology and host cell migration into the implant. With C6-ARSs, stable gas bubbles remained trapped within the fibrin matrix, which inhibited cell migration irrespective of the pattern of ADV. Conversely with C8-ARSs, the release of bFGF in combination with the lack of stable gas bubble formation enabled cell migration that spatially correlated with the pattern of ADV. Significantly greater cell proliferation and angiogenesis was seen in tissues adjacent to +ADV regions of both C6- and C8-ARSs compared to −ADV regions. With C6-ARSs, there was a correlation between angiogenesis and perfusion evaluated by LASCA imaging. Overall, these results demonstrate how regenerative processes like angiogenesis can be spatially directed using ARSs.

Supplementary Material

Refer to Web version on PubMed Central for supplementary material.

Acknowledgments

This work was supported by NIH Grant R01HL139656 (M.L.F.). L.H. was supported by funds the National Key R&D Program of China. Special thanks to Dr. Allen Brooks (Department of Radiology) for assisting with the synthesis of the fluorosurfactant, Aniket Jivani (Department of Radiology) for the CAD designs of the holder for the US transducer, and Dr. William Weadock (Department of Radiology) for helping with 3D printing of CAD designs. Additionally, we thank Dr. Hai Jin for his contributions related staining and analysis of histological images.

References

[1]. Orr AW, Elzie CA, Kucik DF, Murphy-Ullrich JE, Thrombospondin signaling through the calreticulin/LDL receptor-related protein co-complex stimulates random and directed cell migration, Journal of cell science 116(Pt 14) (2003) 2917–27. [PubMed: 12808019]

[2]. Zarem HA, The microcirculatory events within full-thickness skin allografts (homografts) in mice, Surgery 66(2) (1969) 392–7. [PubMed: 4894474]

[3]. Chung YI, Kim SK, Lee YK, Park SJ, Cho KO, Yuk SH, Tae G, Kim YH, Efficient revascularization by VEGF administration via heparin-functionalized nanoparticle-fibrin complex, Journal of Controlled Release 143(3) (2010) 282–289. [PubMed: 20093158]

[4]. Lei Y, Rahim M, Ng Q, Segura T, Hyaluronic acid and fibrin hydrogels with concentrated DNA/PEI polyplexes for local gene delivery, Journal of controlled release : official journal of the Controlled Release Society 153(3) (2011) 255–61. [PubMed: 21295089]

[5]. Grainger SJ, Carrion B, Ceccarelli J, Putnam AJ, Stromal Cell Identity Influences the In Vivo Functionality of Engineered Capillary Networks Formed by Co-delivery of Endothelial Cells and Stromal Cells, Tissue Eng Pt A 19(9–10) (2013) 1209–1222.

[6]. Friend NE, Rioja AY, Kong YP, Beamish JA, Hong X, Habif JC, Bezenah JR, Deng CX, Stegemann JP, Putnam AJ, Injectable pre-cultured tissue modules catalyze the formation of extensive functional microvasculature in vivo, Sci Rep 10(1) (2020) 15562. [PubMed: 32968145]

[7]. Chen RR, Silva EA, Yuen WW, Mooney DJ, Spatio-temporal VEGF and PDGF delivery patterns blood vessel formation and maturation, Pharmaceutical research 24(2) (2007) 258–64. [PubMed: 17191092]

[8]. Leslie-Barbick JE, Moon JJ, West JL, Covalently-immobilized vascular endothelial growth factor promotes endothelial cell tubulogenesis in poly(ethylene glycol) diacrylate hydrogels, J Biomater Sci Polym Ed 20(12) (2009) 1763–79. [PubMed: 19723440]

[9]. Hanjaya-Putra D, Wong KT, Hirotsu K, Khetan S, Burdick JA, Gerecht S, Spatial control of cell-mediated degradation to regulate vasculogenesis and angiogenesis in hyaluronan hydrogels, Biomaterials 33(26) (2012) 6123–6131. [PubMed: 22672833]

[10]. Zhou X, Nowicki M, Sun H, Hann SY, Cui HT, Esworthy T, Lee JD, Plesniak M, Zhang LG, 3D Bioprinting-Tunable Small-Diameter Blood Vessels with Biomimetic Biphasic Cell Layers, Acs Appl Mater Inter 12(41) (2020) 45904–45915.

[11]. Mirabella T, MacArthur JW, Cheng D, Ozaki CK, Woo YJ, Yang MT, Chen CS, 3D-printed vascular networks direct therapeutic angiogenesis in ischaemia, Nat Biomed Eng 1(6) (2017).

[12]. Garvin KA, Hocking DC, Dalecki D, Controlling the spatial organization of cells and extracellular matrix proteins in engineered tissues using ultrasound standing wave fields, Ultrasound Med Biol 36(11) (2010) 1919–32. [PubMed: 20870341]

[13]. Bouyer C, Chen P, Guven S, Demirtas TT, Nieland TJ, Padilla F, Demirci U, A Bio-Acoustic Levitational (BAL) Assembly Method for Engineering of Multilayered, 3D Brain-Like Constructs, Using Human Embryonic Stem Cell Derived Neuro-Progenitors, Adv Mater 28(1) (2016) 161–7. [PubMed: 26554659]

[14]. Kang B, Shin J, Park HJ, Rhyou C, Kang D, Lee SJ, Yoon YS, Cho SW, Lee H, High-resolution acoustophoretic 3D cell patterning to construct functional collateral cylindroids for ischemia therapy, Nat Commun 9(1) (2018) 5402. [PubMed: 30573732]

[15]. Moncion A, Arlotta KJ, Kripfgans OD, Fowlkes JB, Carson PL, Putnam AJ, Franceschi RT, Fabiilli ML, Design and Characterization of Fibrin-Based Acoustically Responsive Scaffolds for Tissue Engineering Applications, Ultrasound Med Biol 42(1) (2016) 257–71. [PubMed: 26526782]

[16]. Fabiilli ML, Wilson CG, Padilla F, Martin-Saavedra FM, Fowlkes JB, Franceschi RT, Acoustic droplet-hydrogel composites for spatial and temporal control of growth factor delivery and scaffold stiffness, Acta Biomater 9(7) (2013) 7399–409. [PubMed: 23535233]

[17]. Fabiilli ML, Lee JA, Kripfgans OD, Carson PL, Fowlkes JB, Delivery of water-soluble drugs using acoustically-triggered, perfluorocarbon double emulsions, Pharmaceutical research 27(12) (2010) 2753–2765. [PubMed: 20872050]

[18]. Kripfgans OD, Fowlkes JB, Miller DL, Eldevik OP, Carson PL, Acoustic droplet vaporization for therapeutic and diagnostic applications, Ultrasound Med Biol 26(7) (2000) 1177–1189. [PubMed: 11053753]

[19]. Kripfgans OD, Fabiilli ML, Carson PL, Fowlkes JB, On the acoustic vaporization of micrometer-sized droplets, Journal of the Acoustical Society of America 116(1) (2004) 272–281.

[20]. Li DS, Kripfgans OD, Fabiilli ML, Brian Fowlkes J, Bull JL, Initial nucleation site formation due to acoustic droplet vaporization, Applied physics letters 104(6) (2014) 063703. [PubMed: 24711671]

[21]. Lu X, Dong X, Natla S, Kripfgans OD, Fowlkes JB, Wang X, Franceschi R, Putnam AJ, Fabiilli ML, Parametric Study of Acoustic Droplet Vaporization Thresholds and Payload Release From Acoustically-Responsive Scaffolds, Ultrasound Med Biol 45(9) (2019) 2471–2484. [PubMed: 31235205]

[22]. Aliabouzar M, Kripfgans OD, Wang WY, Baker BM, Fowlkes JB, Fabiilli ML, Stable and transient bubble formation in acoustically-responsive scaffolds by acoustic droplet vaporization: theory and application in sequential release, Ultrasonics sonochemistry in press (2021).

[23]. Presta M, Maier JA, Rusnati M, Ragnotti G, Basic fibroblast growth factor: production, mitogenic response, and post-receptor signal transduction in cultured normal and transformed fetal bovine aortic endothelial cells, J Cell Physiol 141(3) (1989) 517–26. [PubMed: 2556410]

[24]. Arkudas A, Tjiawi J, Bleiziffer O, Grabinger L, Polykandriotis E, Beier JP, Sturzl M, Horch RE, Kneser U, Fibrin gel-immobilized VEGF and bFGF efficiently stimulate angiogenesis in the AV loop model, Mol Med 13(9–10) (2007) 480–7. [PubMed: 17762899]

[25]. Simons M, Annex BH, Laham RJ, Kleiman N, Henry T, Dauerman H, Udelson JE, Gervino EV, Pike M, Whitehouse MJ, Moon T, Chronos NA, Pharmacological treatment of coronary artery disease with recombinant fibroblast growth factor-2: double-blind, randomized, controlled clinical trial, Circulation 105(7) (2002) 788–93. [PubMed: 11854116]

[26]. Morimoto N, Yoshimura K, Niimi M, Ito T, Aya R, Fujitaka J, Tada H, Teramukai S, Murayama T, Toyooka C, Miura K, Takemoto S, Kanda N, Kawai K, Yokode M, Shimizu A, Suzuki S, Novel collagen/gelatin scaffold with sustained release of basic fibroblast growth factor: clinical trial for chronic skin ulcers, Tissue engineering. Part A 19(17–18) (2013) 1931–40. [PubMed: 23541061]

[27]. Edelman ER, Nugent MA, Karnovsky MJ, Perivascular and intravenous administration of basic fibroblast growth factor: vascular and solid organ deposition, Proceedings of the National Academy of Sciences of the United States of America 90(4) (1993) 1513–7. [PubMed: 8434012]

[28]. Lazarous DF, Scheinowitz M, Shou M, Hodge E, Rajanayagam S, Hunsberger S, Robison WG Jr., Stiber JA, Correa R, Epstein SE, et al., Effects of chronic systemic administration of basic fibroblast growth factor on collateral development in the canine heart, Circulation 91(1) (1995) 145–53. [PubMed: 7805195]

[29]. Moncion A, Lin M, O'Neill EG, Franceschi RT, Kripfgans OD, Putnam AJ, Fabiilli ML, Controlled release of basic fibroblast growth factor for angiogenesis using acoustically-responsive scaffolds, Biomaterials 140 (2017) 26–36. [PubMed: 28624705]

[30]. Dong X, Lu X, Kingston K, Brewer E, Juliar BA, Kripfgans OD, Fowlkes JB, Franceschi RT, Putnam AJ, Liu Z, Fabiilli ML, Controlled delivery of basic fibroblast growth factor (bFGF) using acoustic droplet vaporization stimulates endothelial network formation, Acta Biomater 97 (2019) 409–419. [PubMed: 31404713]

[31]. Lu X, Jin H, Quesada C, Farrell EC, Huang LD, Aliabouzar M, Kripfgans OD, Fowlkes JB, Franceschi RT, Putnam AJ, Fabiilli ML, Spatially-directed cell migration in acoustically-responsive scaffolds through the controlled delivery of basic fibroblast growth factor, Acta Biomater 113 (2020) 217–227. [PubMed: 32553916]

[32]. Ruifrok AC, Johnston DA, Quantification of histochemical staining by color deconvolution, Anal Quant Cytol 23(4) (2001) 291–299.

[33]. Feng Y, Qin D, Zhang J, Zhang L, Bouakaz A, Wan MX, Occlusion and rupture of ex vivo capillary bifurcation due to acoustic droplet vaporization, Applied physics letters 112(23) (2018).

[34]. Kang ST, Yeh CK, Intracellular Acoustic Droplet Vaporization in a Single Peritoneal Macrophage for Drug Delivery Applications, Langmuir 27(21) (2011) 13183–13188. [PubMed: 21936541]

[35]. Radhakrishnan K, Holland CK, Haworth KJ, Scavenging dissolved oxygen via acoustic droplet vaporization, Ultrasonics sonochemistry 31 (2016) 394–403. [PubMed: 26964964]

[36]. Aliabouzar M, Davidson CD, Wang WY, Kripfgans OD, Franceschi RT, Putnam AJ, Fowlkes JB, Baker BM, Fabiilli ML, Spatiotemporal control of micromechanics and microstructure in acoustically-responsive scaffolds using acoustic droplet vaporization, Soft Matter 16(28) (2020) 6501–6513. [PubMed: 32597450]

[37]. Aliabouzar M, Jivani A, Lu XF, Kripfgans OD, Fowlkes JB, Fabiilli ML, Standing wave-assisted acoustic droplet vaporization for single and dual payload release in acoustically-responsive scaffolds, Ultrasonics sonochemistry 66 (2020).

[38]. Moncion A, Arlotta KJ, O'Neill EG, Lin M, Mohr LA, Franceschi RT, Kripfgans OD, Putnam AJ, Fabiilli ML, In vitro and in vivo assessment of controlled release and degradation of acoustically-responsive scaffolds, Acta Biomater 46 (2016) 221–33. [PubMed: 27686040]

[39]. Arkudas A, Tjiawi J, Saumweber A, Beier JP, Polykandriotis E, Bleiziffer O, Horch RE, Kneser U, Evaluation of blood vessel ingrowth in fibrin gel subject to type and concentration of growth factors, J Cell Mol Med 13(9A) (2009) 2864–74. [PubMed: 18624778]

[40]. Murakami M, Simons M, Fibroblast growth factor regulation of neovascularization, Curr Opin Hematol 15(3) (2008) 215–20. [PubMed: 18391788]

[41]. Yang HS, Bhang SH, Hwang JW, Kim DI, Kim BS, Delivery of Basic Fibroblast Growth Factor Using Heparin-Conjugated Fibrin for Therapeutic Angiogenesis, Tissue Eng Pt A 16(6) (2010) 2113–2119.

[42]. Demirdogen B, Elcin AE, Elcin YM, Neovascularization by bFGF releasing hyaluronic acid-gelatin microspheres: in vitro and in vivo studies, Growth Factors 28(6) (2010) 426–436. [PubMed: 20854186]

[43]. Hsieh JY, Smith TD, Meli VS, Tran TN, Botvinick EL, Liu WF, Differential regulation of macrophage inflammatory activation by fibrin and fibrinogen, Acta Biomater 47 (2017) 14–24. [PubMed: 27662809]

[44]. Zhu Y, Lu X, Dong X, Yuan J, Fabiilli ML, Wang X, LED-Based Photoacoustic Imaging for Monitoring Angiogenesis in Fibrin Scaffolds, Tissue engineering. Part C, Methods 25(9) (2019) 523–531. [PubMed: 31418322]

[45]. Jakobsson A, Nilsson GE, Prediction of sampling depth and photon pathlength in laser Doppler flowmetry, Med Biol Eng Comput 31(3) (1993) 301–7. [PubMed: 8412384]

[46]. Lebherz C, von Degenfeld G, Karl A, Pfosser A, Raake P, Pachmayr F, Scholz D, Kupatt C, Boekstegers P, Therapeutic angiogenesis/arteriogenesis in the chronic ischemic rabbit hindlimb: effect of venous basic fibroblast growth factor retroinfusion, Endothelium 10(4–5) (2003) 257–65. [PubMed: 14660086]

[47]. Draijer M, Hondebrink E, van Leeuwen T, Steenbergen W, Review of laser speckle contrast techniques for visualizing tissue perfusion, Lasers Med Sci 24(4) (2009) 639–51. [PubMed: 19050826]

[48]. Korn C, Augustin HG, Mechanisms of Vessel Pruning and Regression, Dev Cell 34(1) (2015) 5–17. [PubMed: 26151903]

[49]. Ozawa CR, Banfi A, Glazer NL, Thurston G, Springer ML, Kraft PE, McDonald DM, Blau HM, Microenvironmental VEGF concentration, not total dose, determines a threshold between normal and aberrant angiogenesis, The Journal of clinical investigation 113(4) (2004) 516–27. [PubMed: 14966561]

[50]. Haworth KJ, Bader KB, Rich KT, Holland CK, Mast TD, Quantitative Frequency-Domain Passive Cavitation Imaging, IEEE Trans Ultrason Ferroelectr Freq Control 64(1) (2017) 177–191. [PubMed: 27992331]

Statement of Significance

Vascularization is a critical step following implantation of an engineered tissue. The ability to spatially pattern or direct vascularization could be therapeutically beneficial for inosculation and vessel in-growth. However, acellular and cell-based strategies to stimulate vascularization typically do not afford this control. We have developed an ultrasound-based method of spatially-controlling angiogenesis using acellular, composite hydrogels termed acoustically-responsive scaffolds (ARSs). An ARS consists of a fibrin matrix doped with a phase-shift double emulsion (PSDE). An ultrasound-mediated process called acoustic droplet vaporization (ADV) was used to release basic fibroblast growth factor (bFGF), which was initially contained within the PSDE. We demonstrate that spatially-defined patterns of ADV within an ARS can elicit spatially-defined patterns of angiogenesis *in vivo*. Overall, these finding can improve strategies for spatially-controlling vascularization.

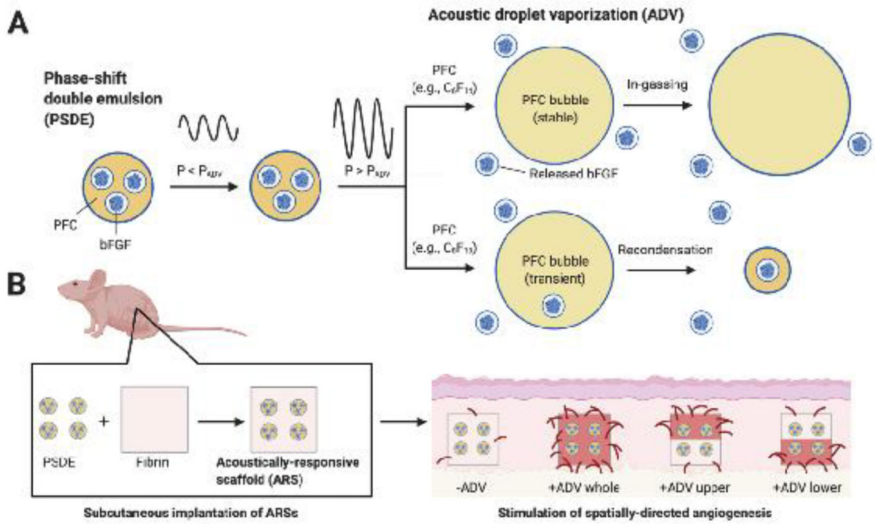

Figure 1.

An ultrasound-based mechanism termed acoustic droplet vaporization (ADV) was used to release basic fibroblast growth factor (bFGF) from an acoustically-responsive scaffold (ARS). A) bFGF was encapsulated within a phase-shift double emulsion (PDSE). At subthreshold acoustic pressures ($P < P_{ADV}$), the perfluorocarbon (PFC) phase within the PSDE remains a liquid. At suprathreshold acoustic pressures ($P > P_{ADV}$), the PFC phase is vaporized into a gas bubble, which causes release of bFGF. Depending on the molecular weight of the PFC, the generated bubble either is stable and continues to grow in size due to in-gassing or is transient and recondenses back into liquid PFC. B) ARSs were generated by incorporating the PSDE into a fibrin hydrogel. The ARSs were exposed *ex situ* to four different spatial patterns of ADV and then implanted subcutaneously in mice. As demonstrated with immunohistochemical staining, angiogenesis correlated with the pattern of ADV. The figure was created with BioRender.com

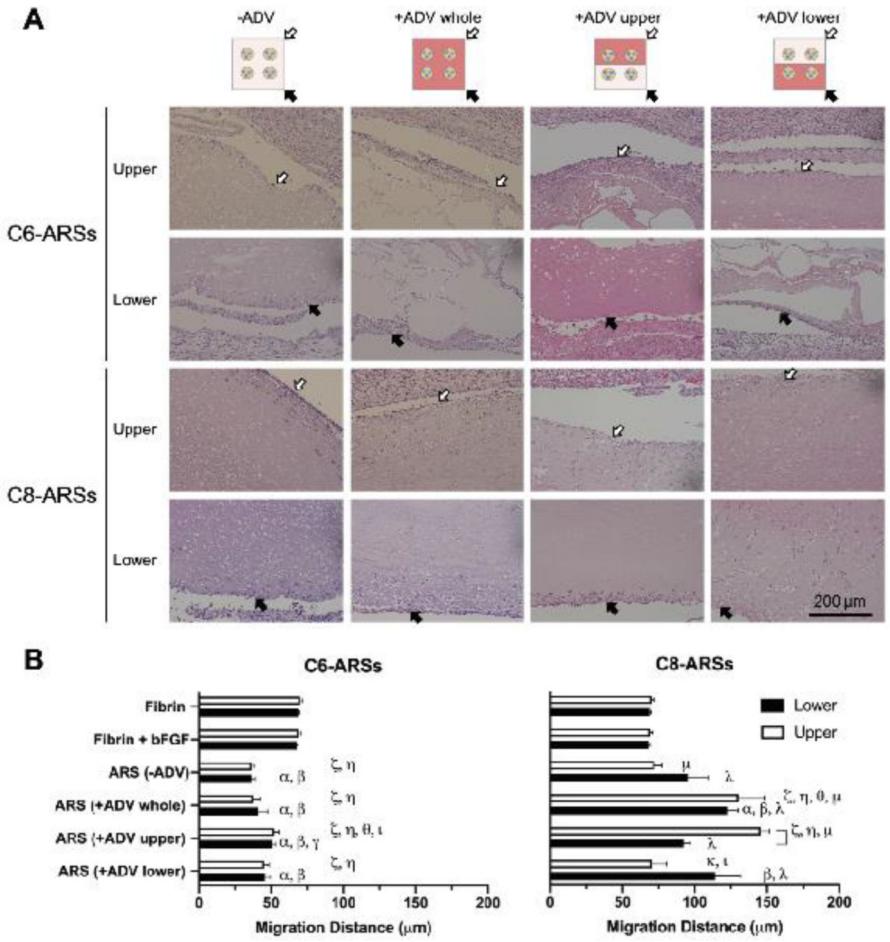

Figure 2.

The morphology of the ARS after ADV and extent of host cell migration into the ARS were dependent on the PFC species within the PSDE and pattern of ADV. A) H&E images of ARSs explanted after 14 days reveal stable bubbles in C6-ARSs whereas no stable bubbles were evident in C8-ARSs. Host cell migration was more evident in C8-ARSs. The white and black arrows denote the upper and lower interfaces of the ARSs proximal to the overlying skin and underlying muscle, respectively. Low magnification images are shown in Supplemental Figure 2. B) The migration distance of host cells into the upper and lower regions of the implanted scaffolds was quantified based on the H&E images. Data are represented as mean ± standard error of the mean (N=5 per group). Significant differences ($p < 0.05$) are denoted by brackets and Greek letters, which are defined in section 2.7.

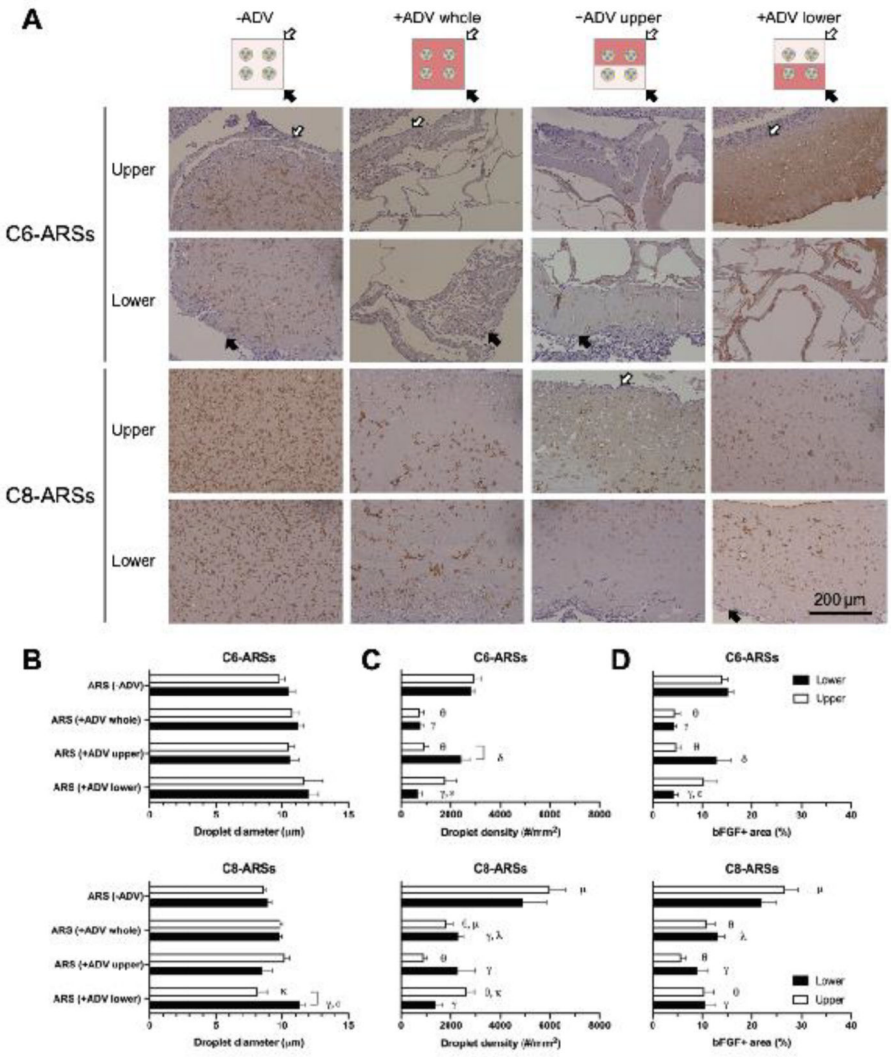

Figure 3.

ADV impacted the size and density of the PSDE within the ARSs. A) Tissue sections were immunohistochemically stained for bFGF and counterstained with hematoxylin. The white and black arrows denote the upper and lower interfaces of the ARSs proximal to the overlying skin and underlying muscle, respectively. Low magnification images are shown in Supplemental Figure 3. The droplet diameter (B), droplet density (C), and bFGF+ area percent (D) were quantified in upper and lower regions of the ARSs. Data are represented as mean ± standard error of the mean (N=5 per group). Significant differences ($p < 0.05$) are denoted by brackets and Greek letters, which are defined in section 2.7.

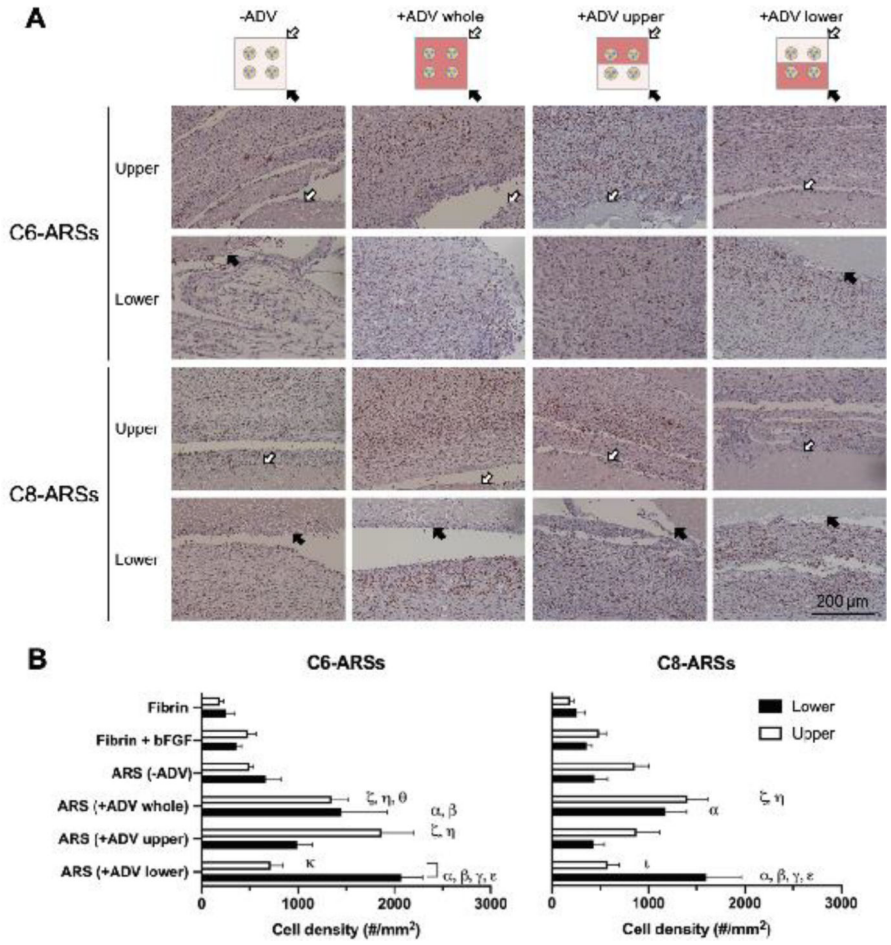

Figure 4.

Cell proliferation around the ARSs correlated with the pattern of ADV. A) Tissue sections were immunohistochemically stained for Ki-67 and counterstained with hematoxylin. The white and black arrows denote the upper and lower interfaces of the ARSs proximal to the overlying skin and underlying muscle, respectively. Low magnification images are shown in Supplemental Figure 4. B) The density of Ki-67+ cells was quantified in adjacent tissues in regions above (i.e., upper) and below (i.e., lower) the implants. Data are represented as mean ± standard error of the mean (N=5 per group). Significant differences ($p < 0.05$) are denoted by brackets and Greek letters, which are defined in section 2.7.

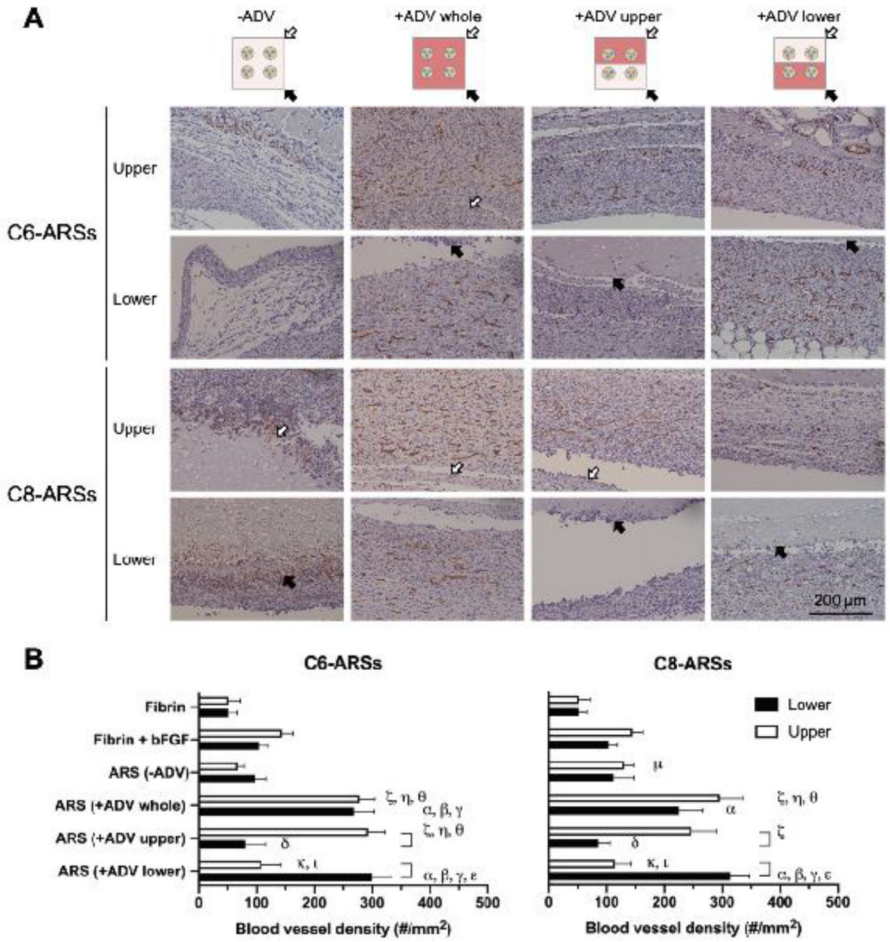

Figure 5.

Angiogenesis around the ARSs correlated with the pattern of ADV. A) Tissue sections were immunohistochemically stained for CD31 and counterstained with hematoxylin. The white and black arrows denote the upper and lower interfaces of the ARSs proximal to the overlying skin and underlying muscle, respectively. Low magnification images are shown in Supplemental Figure 5. B) The density of CD31+ blood vessels was quantified in adjacent tissues in regions above (i.e., upper) and below (i.e., lower) the implants. Data are represented as mean ± standard error of the mean (N=5 per group). Significant differences ($p < 0.05$) are denoted by brackets and Greek letters, which are defined in section 2.7.

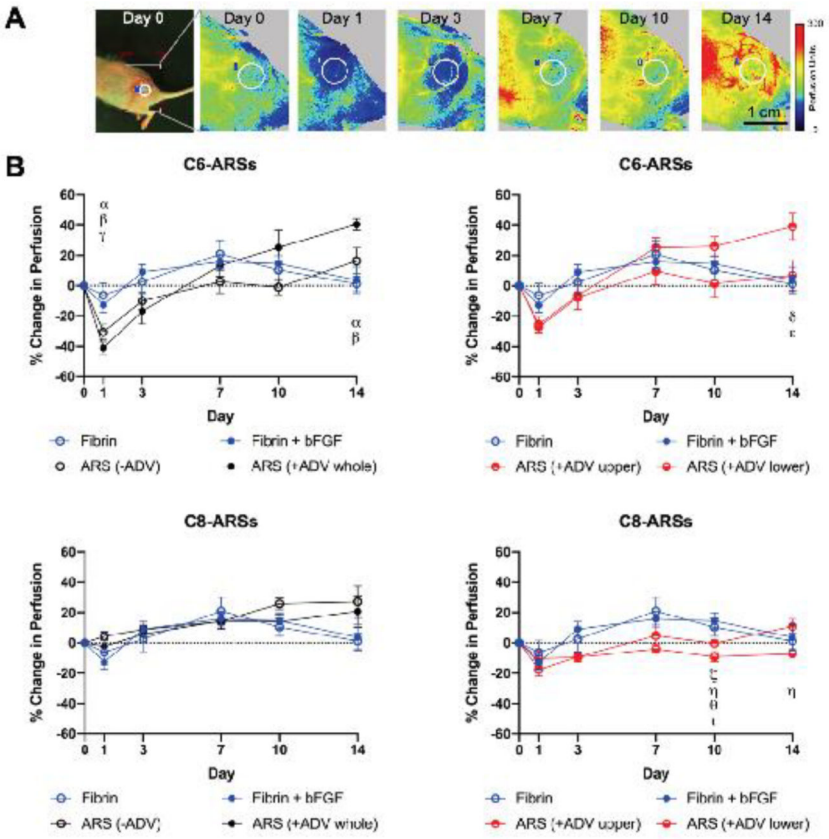

Figure 6.

Laser speckle contrast analysis (LASCA) imaging was used to monitor perfusion in the implant region. A) Longitudinal images display an implanted C6-ARS (+ADV whole) within a mouse, which was imaged in a lateral recumbent position. The white circle denotes the region of interest (ROI) that was used for quantitative analysis. B) The change in perfusion was quantified by calculating the average perfusion within an ROI at a given day and then comparing it to the average perfusion on day 0. Data are represented as mean ± standard error of the mean (N=5 per group). Significant differences ($p < 0.05$) are denoted by Greek letters, which are defined in section 2.7.